Dynamical Meteorology: Atmospheric Tides

F. Gasperini[a] **and J. Oberheide**[b]**,** [a] Orion Space Solutions, Louisville, CO, United States; and [b] Clemson University, Clemson, SC, United States

This is an update of J. Oberheide, M.E. Hagan, A.D. Richmond, J.M. Forbes, DYNAMICAL METEOROLOGY | Atmospheric Tides, Editor(s): Gerald R. North, John Pyle, Fuqing Zhang, Encyclopedia of Atmospheric Sciences (Second Edition), Academic Press, 2015, Pages 287–297, ISBN 9780123822253, https://doi.org/10.1016/B978-0-12-382225-3.00409-6.

Key Points

- Atmospheric tides are oscillations arising due to the rotation of the Earth with respect to the Sun and Moon.
- Solar thermal tides with periods of 24 hours are mainly excited by the absorption of solar radiation and by the release of latent heat associated with the diurnal cycle of tropical convection.
- Lunar gravitational tides are excited by the centrifugal and gravitational forces on the atmosphere associated with the Earth-Moon system.
- Tides are among the most striking dynamical features in the mesosphere and thermosphere and significantly impact the ionosphere.
- Tides in the ionosphere are spatiotemporal variations in electric fields, currents, and plasma density in the ionosphere primarily due to dynamo effects generated by solar and lunar tidal motions in the neutral background atmosphere.
- Tides can interact nonlinearly with each other and with longer-period global-scale waves to produce secondary waves that propagate from their source regions as independent waves, each contributing additional spatial-temporal variability to the system.
- Tides exhibit substantial temporal variability that extends from seasonal and inter-seasonal to intra-seasonal and day-to-day time scales.
- Improved prediction of the ionosphere-thermosphere system is uniquely tied to characterizing tides and their variability through combined theoretical, modeling, and observational studies.

Synopsis

Atmospheric tides are planetary-scale wave motions in the neutral atmosphere with periods defined by Earth's rotation rate. They are among the most striking dynamical features in the mesosphere and thermosphere responsible for redistributing ionospheric plasma through dynamo processes. This article reviews the salient features of atmospheric tides from theoretical, observational, and modeling perspectives, including the recent discovery that tides play a crucial role in connecting planetary-scale weather patterns in the lower atmosphere with the "space weather" of the ionosphere-thermosphere system.

Introduction

Atmospheric tides are ubiquitous features of the Earth's atmosphere. They are the persistent global oscillations that are observed in all types of atmospheric fields, including wind, temperature, pressure, density, and geopotential height. Tidal oscillations have periods that are some integer fraction of a solar or lunar day (Chapman and Lindzen, 1970; Matsushita 1967a,b; Forbes 1995; Hagan et al., 1995). The solar diurnal and semidiurnal tides have 24 and 12 h periods, respectively. The lunar diurnal tidal period is about 24.8 h, while the lunar semidiurnal period is 12.4 h. Scientists often use a shorthand notation to represent solar and lunar tides. S1 and S2 refer respectively to the solar diurnal and semidiurnal tides. Their lunar counterparts are M1 and M2.

Atmospheric tides have been studied for many years as they are evident in both surface pressure and magnetic observations (e.g., Fejer 1964; Tarpley, 1970a,b; Richmond, 1971; Forbes and Lindzen, 1976a,b). **Fig. 1** illustrates a time series of surface pressure measurements made at Batavia (now known as Jakarta, Indonesia) during January 1–5, 1925. The dominant feature of this time series provides evidence of the solar semidiurnal atmospheric tide. Specifically, there is a 1 to 2-hPa deviation from the average pressure of about 1011 hPa that occurs regularly at 12 h intervals. This semidiurnal variation is modulated by other variations, but the former is such a persistent oscillation that the semidiurnal tide is also the dominant oscillation in monthly, yearly, and even multiyear averages of daily surface pressure measurements made at Batavia.

Atmospheric tides are further characterized by their sources. The Moon's gravity forces the lunar atmospheric tide, while solar atmospheric tides can be excited in several ways, including the absorption of solar radiation, large-scale latent heat release associated with deep convective clouds in the troposphere, the gravitational pull of the Sun, and as secondary waves due to nonlinear wave–wave interactions. The restoring force that acts on atmospheric tides is gravity, so tides are a special class of buoyancy or gravity waves. Unlike high-frequency gravity waves, tides are affected by the Earth's rotation and sphericity because of their comparatively long periodicities and large horizontal scales. Amplitudes of solar atmospheric tides are generally larger than lunar tides and dominate the tidal motions in the middle and upper atmosphere, that is, the stratosphere, mesosphere, and thermosphere. Movie 1 illustrates the combined diurnal and semidiurnal tidal motions caused by solar atmospheric tides in the lower thermosphere. Temperature and wind speeds can vary by more than 60 K and >100 m s^{-1} within a few hours.

The general mathematical expression for a tidal oscillation is given by **Eq. (1)**, where A is the magnitude of the variation in some atmospheric field, σ is its frequency, t is universal time, λ is longitude, and $s \geq 0$ is the zonal wavenumber (the number of wave crests that occur along a latitude circle). The $(s\lambda - \sigma t)$ form of **Eq. (1)** is chosen so that the sign of σ is indicative of the zonal direction of propagation: $\sigma > 0$ corresponds to eastward propagating waves and $\sigma < 0$ to westward propagating waves. φ is the so-called tidal phase. A crest of the wave occurs when **Eq. (2)** is satisfied.

$$A\cos(s\lambda - \sigma t - \varphi) \quad [1]$$

$$\varphi = s\lambda - \sigma t \quad [2]$$

The horizontal phase speed of the tide, c_{ph}, is defined by differentiating **Eq. (2)** (**Eqs. 3 and 4**).

$$s\partial\lambda - \sigma\partial t = 0 \quad [3]$$

$$c_{\mathrm{ph}} \equiv \frac{\partial\lambda}{\partial t} = \frac{\sigma}{s} \quad [4]$$

For solar tides, the mth harmonic frequency is $\sigma_m = m\sigma_1$, where m is a positive or negative integer and $\sigma_1 = (2\pi/24)$ h^{-1}. Rewriting the mathematical expression for a tide in terms of LT (hours), $t_{\mathrm{L}} = t + \lambda/\sigma_1$, results in a mathematical expression of the form of **Eq. (5)**.

$$A\cos((s+m)\lambda - \sigma_m t_L - \varphi) \quad [5]$$

For the subset of atmospheric tides known as migrating solar tides, $s = -m$ (with $m < 0$) and **Eq. (5)** reduces to **Eq. (6)**.

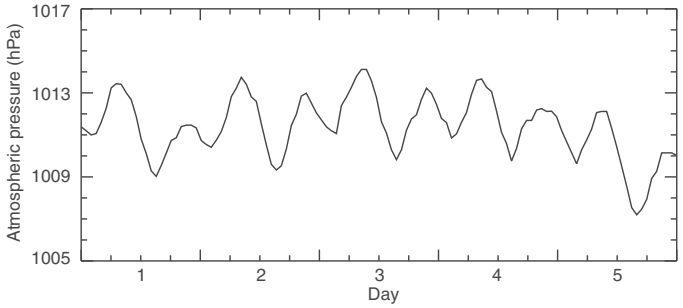

Fig. 1 Surface pressure (hPa) at Batavia (Jakarta, Indonesia) against time during the first 5 days of January 1925.

$$A\cos(|m|\sigma_1 t_L - \varphi) \quad [6]$$

Thus, migrating solar tides have the same local time variation at all longitudes. If $m = -1$ and $s = 1$, the tide is diurnal and moves or migrates westward in longitude with the apparent motion of the Sun from the perspective of a ground-based observer. Further, $c_{ph} = -(2\pi/24)\ h^{-1}$. Similarly, if $m = -2$ and $s = 2$, then the wave is a migrating semidiurnal tide. The remaining set of global-scale waves with tidal periods that are not Sun-synchronous are known as nonmigrating tides. Nonmigrating tides may be viewed as waves that propagate to the west more rapidly or slowly than the Sun, or that propagate eastward, or that are standing. Migrating and nonmigrating solar tides are often identified by using a letter/number code that indicates frequency, propagation direction, and zonal wavenumber: DWs or DEs is a westward or eastward propagating diurnal tide, respectively, with positive zonal wavenumber s. For semidiurnal tides, D is replaced by S, and D0, S0 are standing diurnal and semidiurnal tides, respectively. With this nomenclature, the migrating diurnal (semidiurnal) tide is DW1 (SW2) and DE3, for example, is an eastward propagating diurnal tide of zonal wavenumber 3.

All tides contain components that propagate in the vertical direction z. The effects of upward-propagating tidal components are particularly important because these waves grow in amplitude $\sim\exp(z/2H)$ with scale height H ($=k_B T/Mg$ where k_B is the Boltzmann constant, T is temperature, M is the mean molecular mass, and g is Earth's gravity acceleration) as they conserve energy in an atmosphere whose density decreases with increasing altitude. Thus, tides with insignificant amplitudes in their lower atmospheric regions of excitation often affect the upper atmosphere profoundly because they introduce large atmospheric variations with local time and because they may dissipate and deposit their energy and momentum therein.

Classical Tidal Theory

Classical tidal theory treats tides as perturbations on a basic state with neither mean-flow nor horizontal temperature gradients in an inviscid atmosphere. It provides a reasonable description of atmospheric tides in the lower and middle atmosphere, including the mesosphere and is therefore quite useful to demonstrate important tidal characteristics. As described in detail by Chapman and Lindzen (1970), the linearized primitive equations (Dynamical Meteorology: Primitive Equations) for wave motions described by Eq. (1) and given (s, σ) can be reduced to a single equation for, for example, geopotential. The resulting equation is separable in its latitude and altitude dependence. The latitudinal part is described by Laplace's tidal equation and solved by a complete orthogonal set of eigenfunctions (called Hough modes) and eigenvalues or separation constants (called equivalent depths).

Each Hough mode $\Theta_n^{s,\sigma}$ is a series of associated Legendre polynomials with $|n| \geq s$ being the so-called meridional index because it provides information on the number of latitudinal nodes and symmetry characteristics. It is quite common to refer to a specific Hough mode as the Θ_n^s mode or simply the (s,n) mode and to provide the frequency information externally. The equivalent depth $h_n^{s,\sigma}$ determines the vertical structure of each Hough mode because it is linked to the vertical wavelength λ_z (Eq. 7),

$$\lambda_{z,n}^{s,\sigma} = \frac{2\pi H}{\sqrt{\frac{\left(kH + \frac{d}{dx}H\right)}{h_n^{s,\sigma}} - \frac{1}{4}}} \quad [7]$$

with scale height H, $k = (\gamma - 1)/\gamma$ and adiabatic index $\gamma \approx 7/5$, and normalized height $x = z/H$. Eq. (7) implies that equivalent depths must be positive but smaller than roughly 8 km for vertical wave propagation. Larger values or negative equivalent depths imply vertically trapped modes. Fig. 2 illustrates Hough modes corresponding to the first two propagating and trapped modes of the migrating DW1 and nonmigrating DE3 tides, respectively. Diurnal propagating modes generally maximize at low to middle latitudes and trapped modes at middle to high latitudes.

Symmetric Hough functions are mirror images about the equator and occur if $n + s$ is even (odd) for positive (negative) values of n. Antisymmetric modes change sign at the equator and occur if $n + s$ is odd (even) for positive (negative) n. Tidal variations δF in temperature, pressure, geopotential, density, and vertical wind as function of normalized height x, latitude ϑ, zonal wavenumber s, and frequency σ are described by Eq. (8)

$$\delta F^{s,\sigma}(x,\vartheta) = \sum_n \delta F_n^{s,\sigma}(x)\Theta_n^{s,\sigma}(\vartheta) \quad [8]$$

Zonal (u) and meridional (v) wind variations are described by Eqs. (9) and (10)

$$\delta u^{s,\sigma}(x,\vartheta) = \sum_n \delta u_n^{s,\sigma}(x)U_n^{s,\sigma}(\vartheta) \quad [9]$$

$$\delta v^{s,\sigma}(x,\vartheta) = \sum_n \delta v_n^{s,\sigma}(x)V_n^{s,\sigma}(\vartheta) \quad [10]$$

with the wind expansion functions shown in Fig. 3 (Eqs. 11 and 12)

$$U_n^{s,\sigma}(\vartheta) = \frac{1}{(f^2 - \sin^2\vartheta)}\left[\frac{s}{\cos\vartheta} + \frac{\sin\vartheta}{f}\,d\text{ over }d\,\vartheta\right]\Theta_n^{s,\sigma}(\vartheta) \quad [11]$$

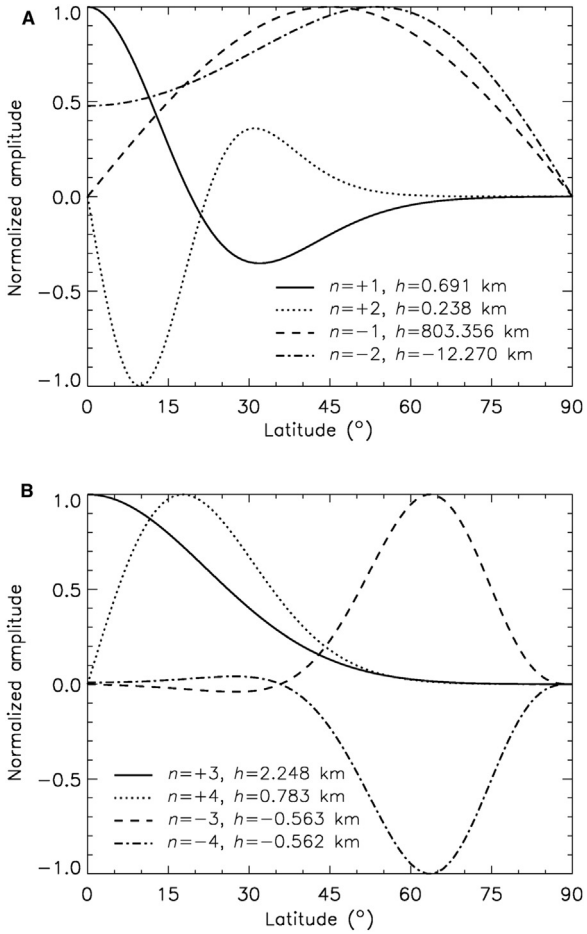

Fig. 2 (A) Hough modes for the migrating diurnal solar tide (DW1). The meridional index n is positive for propagating tides and negative for trapped tides. (B) Same as (A) but for the DE3 nonmigrating tide.

$$V_n^{s,\sigma}(\vartheta) = \frac{1}{\left(f^2 - \sin^2\vartheta\right)}\left[\frac{s\tan\vartheta}{f} + d\,\text{over}\,d\,\vartheta\right]\Theta_n^{s,\sigma}(\vartheta) \qquad [12]$$

with $f = \sigma/(2\Omega)$ and Earth's angular velocity Ω. The zonal wind expansion functions $\boldsymbol{U}_n^{s,\sigma}$ have the same symmetry as the corresponding Hough modes. $\boldsymbol{V}_n^{s,\sigma}$, on the other hand, are symmetric (antisymmetric) when the corresponding Hough modes are antisymmetric (symmetric).

The classical tidal theory approximates the tidal motions in the lower and middle atmosphere reasonably well, including the mesosphere. Classical methods of computing tides, however, do not work when mean zonal winds or dissipation are included, because the mathematical solutions become inseparable in the latitudinal and vertical coordinates. Hough modes are no longer eigenfunctions of the system and numerical solutions are needed. This is particularly important in the thermosphere where the tides undergo a substantial change in their modal structure when molecular dissipation becomes important. This transition height occurs approximately where the dissipative time scale equals the scale height divided by the vertical group velocity. Amplitudes and phases relax to approximately constant values in the thermosphere and the damping significantly broadens the horizontal structure. It should also be noted that the time constants of eddy and molecular diffusion are proportional to the square of λ_z. Short vertical wavelength tides or modes therefore dissipate more rapidly and cannot propagate into the thermosphere at all.

Migrating Solar Tides

The absorption of radiation by a longitudinally invariant atmosphere is the primary source of migrating solar tides. Owing to the rotation of the Earth, this absorption is periodic in time from the perspective of the ground-based observer. The resultant heating gives rise to migrating tidal oscillations. Solar radiation is absorbed throughout the Earth's atmosphere, thereby exciting migrating solar tides at almost all altitudes. Atomic oxygen, which is the most abundant atmospheric constituent at altitudes about 150 km above the Earth's surface, absorbs the shortest-wavelength solar radiation, known as the extreme ultraviolet (EUV). Increasingly

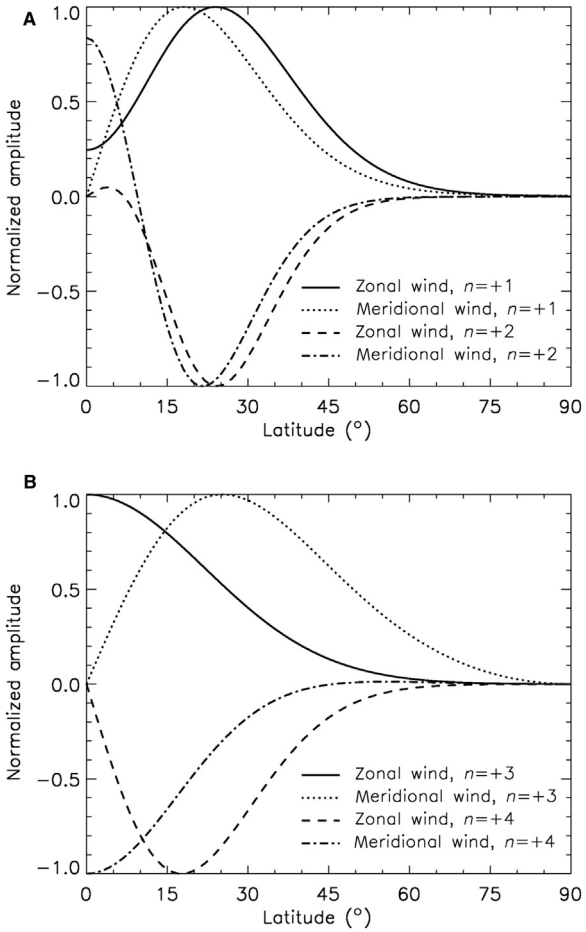

Fig. 3 (A) Wind expansion functions for the migrating diurnal solar tide (DW1). The first two propagating modes are shown. (B) Same as (A) but for the DE3 nonmigrating tide.

longer wavelengths are absorbed as the solar radiation approaches the Earth's surface. Molecular oxygen (O_2) absorbs the far-ultraviolet radiation (FUV, 100−200 nm) at altitudes near about 100−150 km, and ozone (O_3) absorbs the 200 to 300-nm solar ultraviolet radiation (UV) at middle atmospheric altitudes between about 30 and 70 km. Solar infrared (IR) radiation may be absorbed by water vapor (H_2O) in the lowest part of the atmosphere.

Even though there is little, if any, tidal forcing due to solar heating in the upper mesosphere (~80−100 km), measurements of winds and temperatures exhibit strong tidal signatures in this region. Fig. 4 illustrates an example of the magnitude of the mean winds and the tidal oscillations over Adelaide, Australia, at these altitudes. The data points represent the eastward winds that were measured with the Buckland Park radar during 8−9 August 1994. The dashed curves illustrate global-scale wave model (GSWM) tidal predictions for August at the location of Adelaide. While the GSWM differs from the measurements in detail, the model captures the salient features of the observed winds, particularly on 8 August. Differences may be attributable to small-scale waves that are not included in GSWM or to sources of day-to-day tidal variability that are also omitted.

The GSWM predictions include mean winds (17−18 m s^{-1}) and both migrating diurnal and semidiurnal components. Notably, the migrating diurnal amplitudes (20−30 m s^{-1}) are larger than the mean winds. The GSWM diurnal tidal amplitudes are at least a factor of 2 larger than the semidiurnal amplitudes (8−15 m s^{-1}) and the phases of both components shift to earlier times with increasing altitude between 90 and 98 km. This behavior, which is known as downward phase progression, is indicative of upward-propagating wave energy. There are clear signatures of downward phase progression in the GSWM predictions in Fig. 4. That is, the wind predictions are most westward near 15.00 h at 98 km and there are similar features at progressively later times and progressively lower altitudes. The vertical wavelength of the migrating diurnal tide over Adelaide is much shorter than that of the migrating semidiurnal tide, so the phase of the former progresses far more rapidly than the phase of the latter and their combined effects result in a pattern of wave maxima and minima that evolves between altitudes.

The migrating diurnal tide below the mesopause (i.e., the region between the mesosphere and thermosphere near 100 km altitude) originates primarily in the troposphere. Although tropospheric semidiurnal forcing is nonnegligible, there is comparatively more semidiurnal forcing in the middle atmosphere. Thus, the growth of diurnal tides forced near the surface occurs over a deeper altitude region than the semidiurnal growth, and it is reasonable to anticipate a diurnal amplitude that is larger than the semidiurnal

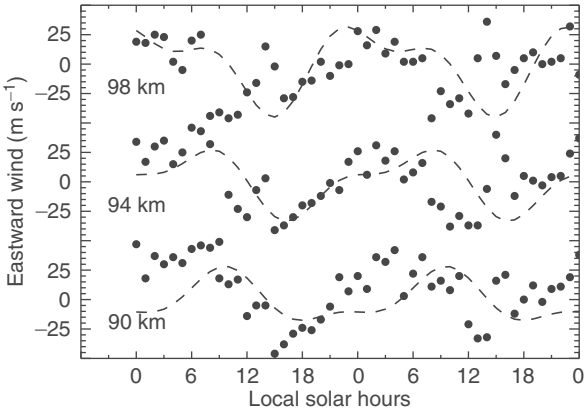

Fig. 4 Eastward winds (m s^{-1}) over Adelaide, Australia, against local time (h) on 8–9 August 1994 at 98 km (top), 94 km (middle), and 90 km (bottom). Data points are radar measurements and dashed curves are model predictions that include the migrating diurnal and semidiurnal tidal components. Professor R.A. Vincent provided the Adelaide radar data.

amplitude in the upper mesosphere. The aggregate characteristics of the mean winds and tides that are illustrated in **Fig. 4** support the claim that upward-propagating migrating tides govern the large-scale dynamics of the upper mesosphere.

Migrating tides exhibit somewhat complicated behavior in that the latitudinal structure of the horizontal wind oscillations is dramatically different from the temperature, pressure, or vertical velocity structure. For example, the upward-propagating migrating diurnal tide DW1 is characterized by a primary temperature amplitude maximum over the Equator with secondary maxima near ±30°. The horizontal wind amplitudes (Movie 2) exhibit minima over the Equator and nearly symmetric amplitude peaks at low to middle latitudes (i.e., ±(20–30)°). While ground-based observations provide an important perspective on the local behavior of waves with tidal frequencies, it is impossible to decipher global structures from local structures without conducting correlative analysis of measurements made at multiple locations over a broad range of latitudes. Further, in order to distinguish migrating from nonmigrating tidal components, it is necessary to have a longitudinal distribution of measurements.

The upward-propagating migrating tides dissipate in the lower thermosphere and their contribution to upper thermosphere variability is comparatively small. However, the longitudinally invariant absorption of solar far and extreme ultraviolet radiation efficiently forces a large *in situ* component of the migrating tides that dramatically changes the temperature, density, and wind structure in the upper thermosphere. **Fig. 5** illustrates its magnitude based on the output from the NRLMSISE-00 (i.e., the 2000 version of the Naval Research Laboratory Mass Spectrometer Incoherent Scatter Radar Extended) empirical model. Local time mass density variations at 400 km at 12:00 Universal Time are on the order of a factor of 3 when the tides (diurnal, semidiurnal, terdiurnal) are included (left panel) but almost nonexistent when the tides are excluded (right panel). The largest tidal signal in **Fig. 5** (left panel) comes from the migrating diurnal tide DW1. It maximizes at the equator (latitude of the subsolar point during equinoxes) and decreases toward higher latitudes along with the noontime solar angle, as expected for an *in situ* forced tide. NRLMSISE-00 does not include nonmigrating tides. Diagnostics of upper thermosphere neutral density observations from the CHAllenging Minisatellite Payload (CHAMP) satellite indicate that nonmigrating tides induce an additional longitudinal variability on the order of 30%–50%, mostly due to upward-propagating tides from the troposphere. An accurate description of migrating and nonmigrating diurnal density variations is especially important for predicting low perigee satellite trajectories because atmospheric drag is the dominant error source in operational models.

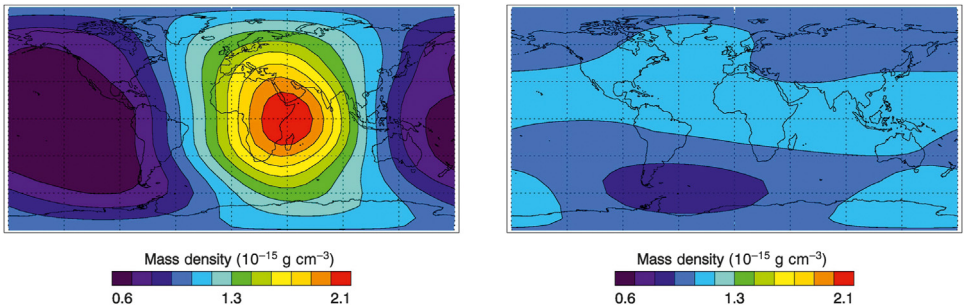

Fig. 5 Global distribution of neutral mass density at 12:00 Universal Time and 400 km altitude on September 21, 2010 with (left) and without (right) thermospheric tides. Data shown are from the NRLMSISE-00 model and do not include nonmigrating tides.

Nonmigrating Tides

Near the surface of the Earth the strong longitudinal differences in topography, land–sea contrast, and surface interactions produce zonal (i.e., along a latitude circle in the east–west direction) variations in the local time behavior of the atmosphere and thus excite nonmigrating tides. A good example is latent heat release due to condensation in large-scale deep convective systems in the tropical troposphere. **Fig. 6** illustrates the latitude–longitude distributions of the diurnal (left) and semidiurnal (right) latent heat release amplitudes during the month of September derived from satellite-borne convective rainfall measurements. Both components maximize at low latitudes where the absorption of solar radiation (evaporation) is greatest. Their longitudinal structure reflects the areas of largest deep convective activity in the tropical troposphere: one peak over Africa, followed by two peaks over Indonesia and the western Pacific and a fourth over South and Central America.

Through Fourier analysis the longitude variations depicted in **Fig. 6** may be decomposed into a series of wave components with different zonal wavenumbers *s*. Each of the resultant nonmigrating tidal components possesses different vertical propagation characteristics that depend on its sensitivity to the prevailing winds and its vertical wavelength. Good examples are the DW5 and DE3 components. Both are efficiently forced by latent heat release but DW5 dissipates at lower altitudes due to its short vertical wavelength. DE3 on the other hand has a long vertical wavelength and propagates up into the lower thermosphere where its magnitude rivals the radiatively forced migrating diurnal tide (Movie 2).

It is difficult to track vertical tidal propagation into the upper atmosphere such as that depicted in Movie 2 because the distribution of ground-based observations is spatially limited and satellite observations are largely asynoptic (i.e., at a given height and latitude, not all UTs are sampled simultaneously across all longitudes), requiring averages over multiple days to cover all local times needed to extract the full tidal spectrum. This is particularly true for altitudes between about 100 km and 180 km above the Earth's surface, which encompass the region where the upward-propagating waves attain large amplitudes and subsequently dissipate. It is generally impossible to distinguish migrating from nonmigrating tides in the analysis of ground-based remote-sensing measurements from a single site made at these altitudes. During the 1990s remote sensing data from the Upper Atmosphere Research Satellite (UARS) considerably ameliorated this problem. Further progress came from the Thermosphere Ionosphere Mesosphere Energetics and Dynamics (TIMED) satellite that was launched in 2001 because it allowed for the first time to observe the global tidal spectrum in various parameters over a range of mesosphere and lower thermosphere altitudes (e.g., Oberheide et al., 2011). The data utilized to construct Movies 1–4 consist of wind measurements made by the TIMED Doppler Interferometer (TIDI) and temperature measurements made by the Sounding the Atmosphere using Broadband Emission Radiometry (SABER) instrument that are extended toward the poles and into the lower atmosphere and upper thermosphere using an empirical tidal model.

Movies 3 and 4 illustrate the latitude–longitude distribution of the diurnal and semidiurnal tides at 100 km for the month of September, averaged over 7 years from 2002 to 2008. The superposition of these movies is shown in Movie 1. The diurnal tide with amplitudes as large as 28 K and 42 m s^{-1}, respectively, mainly consists of the migrating component DW1 and the nonmigrating DE3 tide, with some contributions from the DE2, D0, and DW2 components. The migrating tide is observed as a zonally symmetric oscillation because the movie is animated in LT (compare **Eq. 5**) and the DE3 as a 4-peaked longitudinal variation for the same reason. The semidiurnal tidal field is more symmetric than the diurnal one with amplitudes of 17 K and 36 m s^{-1}, respectively. Spectral analysis of these observations reveals that the longitudinal structure is dominated by the migrating tide SW2, with contributions from the SW3, SW1, and SE2 nonmigrating tides.

Complementary numerical modeling studies suggest that the diurnal and semidiurnal nonmigrating tides are generated in the lower levels of the atmosphere, either by latent heat release (DE3, DE2, SE2) and/or as secondary waves by the nonlinear interaction between stationary planetary waves and the migrating tides (DW2, D0, SW1, SW3). An example from the "Whole Atmosphere Model" (WAM) is shown in **Fig. 7** (Akmaev et al., 2008). WAM is a general circulation model of the neutral atmosphere built on an existing operational Global Forecast Model used by the US National Weather Service. It includes realistic topography and latent heating associated with tropospheric convection and nonlinear processes, and the model domain extends well into the

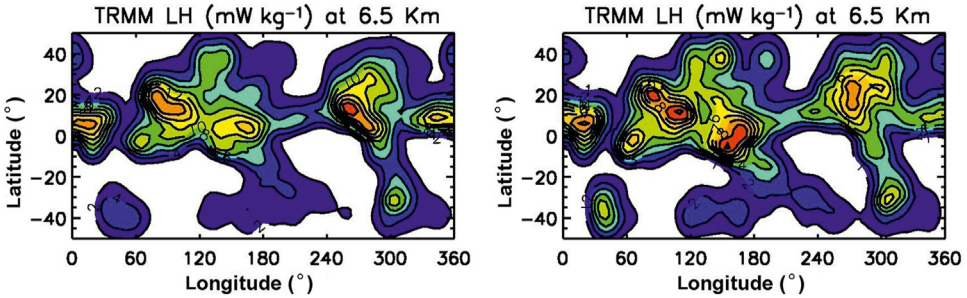

Fig. 6 Contours of diurnal (left) and semidiurnal (right) latent heat release amplitudes in the troposphere from Tropical Rainfall Measuring Mission (TRMM) satellite observations during September. Dr X. Zhang provided these figures, which are adapted with permission from Zhang, X., Forbes, J.M., Hagan, M.E., 2010. Longitudinal variation of tides in the MLT region: 2. Relative effects of solar radiative and latent heating. Journal of Geophysical Research 115, A06317. https://doi.org/10.1029/2009JA014898.

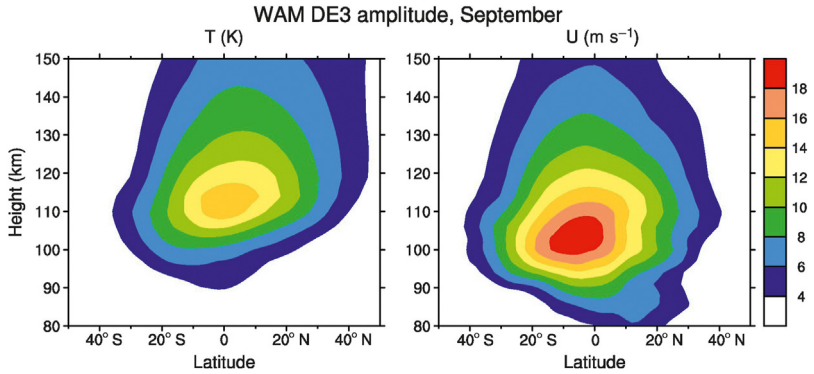

Fig. 7 WAM DE3 amplitude of (left) temperature and (right) zonal wind as a function of latitude and height in September. Dr R.A. Akmaev provided the model results, which are adapted with permission from Akmaev, R.A., Fuller-Rowell, T.J., Wu, F., Forbes, J.M., Zhang, X.Anghel, A.F., Iredell, M.D., Moorthi, S., Juang, H.-M., 2008. Tidal variability in the lower thermosphere: comparison of whole atmosphere model (WAM) simulations with observations from TIMED. Geophys. Res. Lett. 35, L03810. https://doi.org/10.1029/2007GL032584.

dissipative thermosphere to a top level of about 600 km. The WAM temperature and zonal wind components associated with the DE3 tide exhibit maxima centered around the equator that can also be discerned in the TIMED satellite measurements shown in Movie 2.

Lunar Tides

Lunar atmospheric tides are typically only about 5%–10% as large as solar tides, but they have clearly detectable effects (Vial and Forbes, 1994; Zhang and Forbes 2013). The lunar tidal pressure at the ground maximizes at low latitudes, with an average amplitude of about 7 Pa. The corresponding wind amplitude at the Equator is about 0.03 m s^{-1}. The wind amplitude increases with altitude up to about 110 km, where it reaches an amplitude on the order 10 m s^{-1}.

Unlike solar tides, lunar atmospheric tides are entirely driven by gravitational forces, as illustrated schematically in **Fig. 8**. Because the lunar gravitational acceleration decreases as the inverse square of the distance from the center of the Moon, this acceleration is not exactly uniform near the Earth, so that atmospheric air parcels at various locations around the Earth experience slightly different lunar accelerations from those of the Earth as a whole. Air parcels in the hemisphere most distant from the Moon are accelerated toward the Moon less strongly than is the Earth, in effect creating a relative acceleration away from the Moon for these air parcels, in the Earth's reference frame. Conversely, air parcels in the moonward hemisphere of the Earth experience a relative acceleration toward the Moon. In each hemisphere, parcels to the west of a line passing through the centers of the Earth and Moon

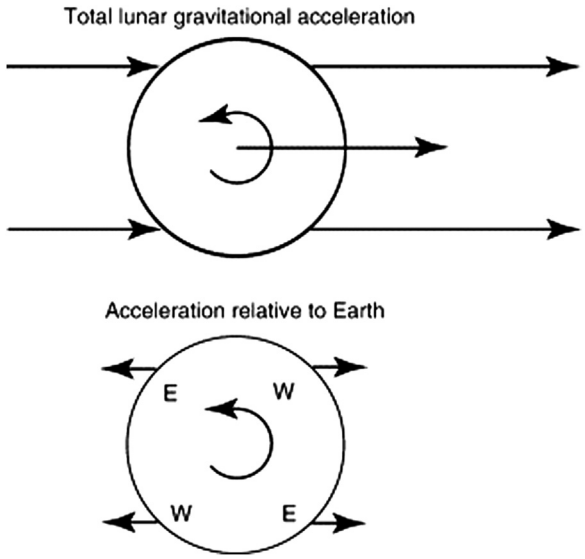

Fig. 8 Schematics of lunar tidal forcing in the reference frames of the Moon (top) and the Earth (bottom). The Earth is viewed from above the North Pole and the Moon (not shown) is to the right.

experience an eastward component of acceleration, while those to the east of this line experience a westward acceleration. As the Earth rotates, during a lunar day (24.8412 h on average) an air parcel at the Equator successively passes twice through regions of westward and eastward acceleration, comprising two lunar semidiurnal cycles of period 12.4206 h. When the Moon is north or south of the Earth's Equator, an additional diurnal lunar cycle (period 24.8412 h) of acceleration exists at nonequatorial latitudes. There is also a monthly periodicity to the forcing as the Moon cycles between the Northern and Southern Hemispheres of the Earth. Both this cycling and the ellipticity of the Moon's orbit create amplitude and frequency modulation of the lunar semidiurnal and diurnal forcings that can be expressed as combinations of multiple closely spaced periods. The dominant lunar period, representing the average lunar semidiurnal tide, is referred to as the M2 tide, with a 12.4206 h period.

In addition to the direct forcing of lunar gravity on the atmosphere, lunar atmospheric tides are indirectly forced by lunar gravity through deformation of the Earth's surface due to ocean and Earth tides. The vertical velocity associated with this deformation significantly affects the atmospheric tide, and the modulation of terrestrial gravity by the deformation of the Earth's mass distribution also has an effect. These indirect forcing effects can be determined accurately from measurements of ocean and Earth tides, so that the total lunar tidal forcing is well known. This is beneficial for testing theoretical models of tidal propagation and dissipation in the atmosphere. The indirect forcing effects, because they depend on land–sea differences, are a function not only of apparent lunar position but also of geographical location, and generate nonmigrating tides in addition to the primary migrating lunar tides.

It is possible to develop a model of the M2 lunar semidiurnal atmospheric tide that produces results that agree very satisfactorily with the observed tide in the surface pressure. Such a model must account for all direct and indirect lunar forcing effects, and include realistic atmospheric wind and temperature structures. Fig. 9 illustrates prototypical M2 model results and shows how the lunar tidal pressure amplitude varies with latitude and longitude over the Earth for atmospheric conditions representing the month of December. Globally, maximum M2 amplitudes generally occur during solstices, with larger values in December than in June. The largest amplitudes in December are at low latitudes, but they vary from less than 4 Pa (40 dPa) on the east coast of South America to more than 12 Pa over the mid-Pacific. A secondary maximum appears over the northern Atlantic. Modeling studies suggest that an important source of M_2 amplification is its proximity (at 12.42 hr) to an atmospheric resonant response that shifts from 12.81 to 12.43 solar hours under Sudden Stratospheric Warming (SSW) conditions (discussed in more detail below).

Atmosphere-Ionosphere Coupling via Solar and Lunar Tides

Tides in the ionosphere are spatiotemporal variations in electric fields, currents, and plasma density primarily due to dynamo effects generated by solar and lunar tidal motions in the neutral background atmosphere (e.g., Richmond, 1995; Immel et al., 2006; Hagan et al., 2007; Scherliess et al., 2008; England et al., 2010; Forbes et al., 2021). Tidal winds in the low and middle latitude E-region move the partially ionized plasma through the Earth's magnetic field while the electrons with their high gyro frequency/collision frequency ratio remain fixed to the magnetic field lines. An electromotive force is thus created with ensuing electric currents and polarization electric fields.

During the daytime, when the conductivity is large owing to ionizing solar radiation, the electric currents, commonly labeled S_q for "solar quiet," flow approximately counterclockwise in the Northern Hemisphere and clockwise in the Southern Hemisphere with vortex foci at roughly ±30° magnetic latitude. A particularly strong eastward current, called equatorial electrojet, exists along the geomagnetic equator because the effective ionospheric conductivity is unusually high in the lower ionosphere at latitudes where the geomagnetic field is nearly horizontal. The S_q currents produce perturbations in the Earth's magnetic field that are readily measured at the ground. The E-region dynamo polarization electric fields are further transmitted along magnetic field lines into the overlying F-region where they drive vertical (~20 m s^{-1}) and zonal (~100 m s^{-1}) plasma drifts, which influence many important ionospheric processes. For example, vertical E x B drifts drive the plasma fountain which results in dense bands of plasma centered near ±15–20° magnetic latitude. This so-called equatorial ionization anomaly (EIA) can be seen in the top center panel

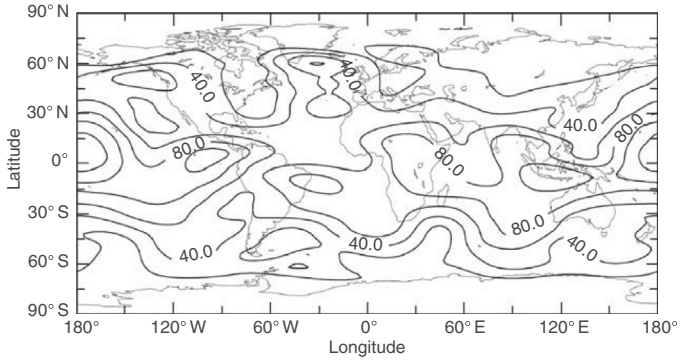

Fig. 9 Contours of M2 lunar semidiurnal surface pressure amplitude (dPa) against longitude and latitude for the month of December. Dr F. Vial collaborated with Professor J.M. Forbes to produce the model results.

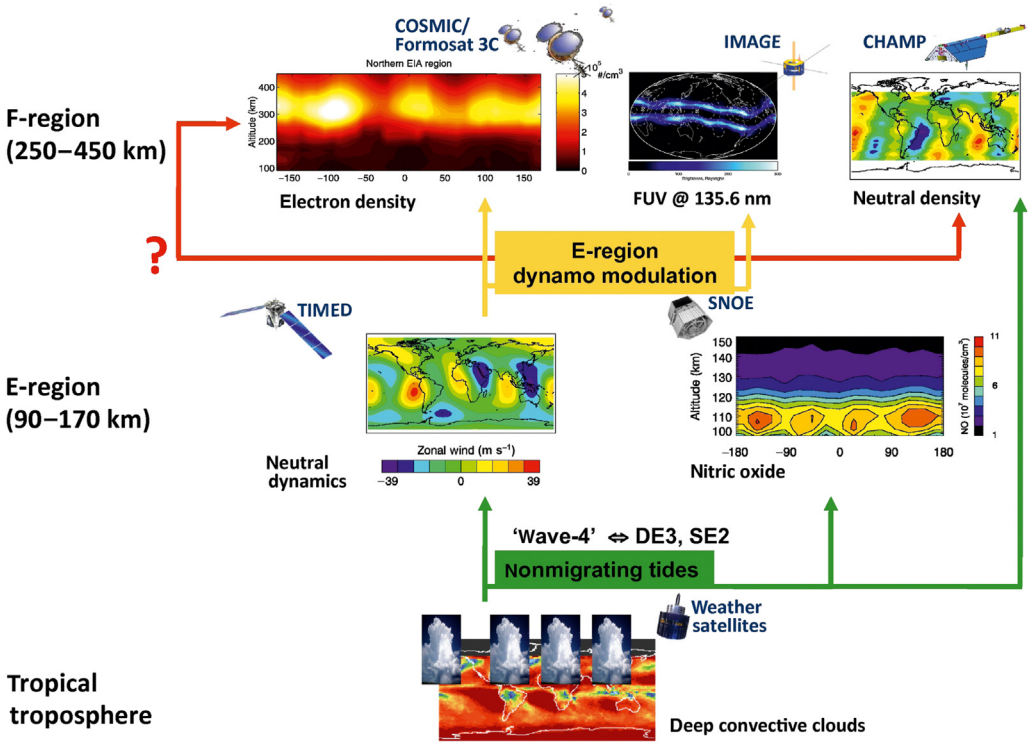

Fig. 10 Meteorological impacts on the ionosphere–thermosphere due to nonmigrating tides as observed by different satellites. The "wave-4" like latent heat release pattern in the troposphere is found throughout the ionosphere–thermosphere system in various neutral and ion parameters. Dr C.H. Lin provided the Constellation Observing System for Meteorology, Ionosphere & Climate (COSMIC) figure, which is adapted with permission from Lin, C.H., et al., 2007. Plausible effect of atmospheric tides on the equatorial ionosphere observed by the FORMOSAT-3/COSMIC: three-dimensional electron density structures. Geophysical Research Letters 34, L11112. https://doi.org/10.1029/2007GL029265. Dr T.J. Immel provided the IMAGE figure, which is adapted with permission from Immel, T.J., et al., 2006. Control of equatorial ionospheric morphology by atmospheric tides. Geophys. Res. Lett. 33, L15108. https://doi.org/10.1029/2006GL026161. Dr X. Zhang and Dr S.L. Bruinsma provided the CHAMP neutral density data. The Student Nitric Oxide Explorer (SNOE) nitric oxide figure is adapted with permission from Oberheide, J., Forbes, J.M., 2008. Thermospheric nitric oxide variability induced by nonmigrating tides. Geophys. Res. Lett. 35, L16814. https://doi.org/10.1029/2008GL034825. Deep tropical cloud data are from the International Satellite Cloud Climatology Project (ISCCP).

in Fig. 10, as the two bluish bands north and south of the magnetic equator. The two ionization crests are predominantly the result of migrating solar tidal winds in the E-region while the apparent longitudinal modulation on top, indicated by brighter colors, is the result of nonmigrating tides excited in the troposphere by latent heat release in deep convective tropical clouds.

The realization that nonmigrating tides due to tropospheric weather impact the F-region ionosphere, and as such couple these atmospheric layers that are 400 km apart, is a relatively new discovery that was made around the year 2005 due to new satellite observations and progress in numerical modeling (e.g., Immel et al., 2006; Lin et al., 2009; Oberheide et al., 2015). Fig. 10 summarizes these observations which are all displayed for a constant LT, and sketches the cause-and-effect chain of meteorological impacts on the IT system. The most striking pattern is a 4-peaked "wave-4" longitudinal modulation that is apparent in deep convective cloud occurrence (observed by weather satellites, also compare Fig. 6), E-region zonal winds (observed by TIMED, also compare Movie 1), thermospheric constituents (observed by the SNOE in equatorial nitric oxide density), electron density (observed by the COSMIC/Formosat-3), ion density (observed by IMAGE spacecraft in the far-ultraviolet), and neutral mass density (observed by CHAMP). The "wave-4" corresponds to the DE3 nonmigrating tide with some contribution from the SE2 (and other tidal components including the stationary planetary wave with s = 4, or SPW4), because this is how these components are observed in a LT frame (Eq. 5). Movie 2 and Fig. 6 show that the DE3 can achieve zonal wind amplitudes on the order of tens of m s^{-1} in the low latitude E-region. It thus efficiently modulates the E-region dynamo electric fields, resulting in the pronounced "wave-4" F-region plasma density variations. All these observations and corresponding model simulations imply that tropospheric weather is an important contributor to the "space weather" of the geomagnetically quiescent ionosphere, even for solar maximum conditions, and capable to change, for example, electron density by a factor of three within a few thousand kilometers.

Longitudinal variations in the ionospheric plasma due to nonmigrating tides do not always occur as a "wave-4." The "wave-4" dominates from March to October but changes to a 3-peaked "wave-3" from November to February when observed at a fixed LT (Fig. 11). This is mainly due to the seasonal variation of the diurnal nonmigrating tides in the E-region as depicted in Fig. 12. The DE3 dominates from March to October but it is exceeded by another component, the DE2 (observed as a "wave-3") during Northern Hemisphere winter.

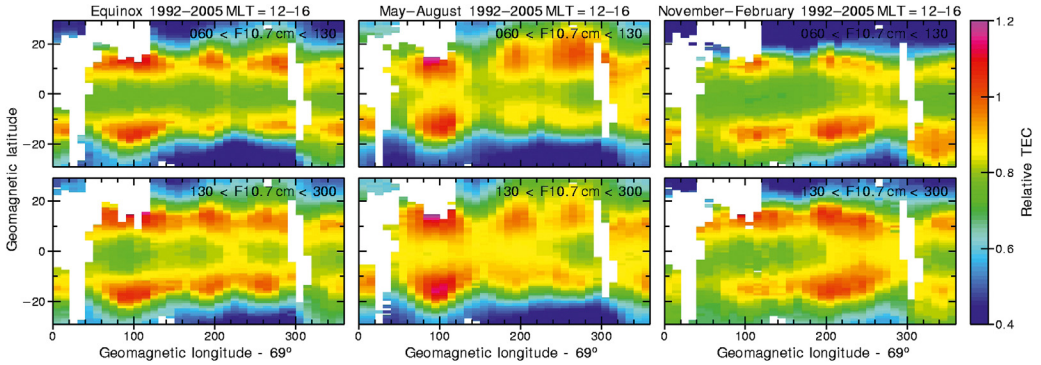

Fig. 11 Seasonal variation of normalized total electron content from TOPEX/Poseidon observations for low (upper row) and high (lower row) solar flux conditions. Professor L. Scherliess provided these figures, which are adapted with permission from Scherliess, L., Thompson, D.C., Schunk, R.W., 2008. Longitudinal variability of low-latitude total electron content: tidal influences. J. Geophys. Res. 113, A01311. https://doi.org/10.1029/2007JA012480.

The lunar tide is a prominent source of atmosphere-ionosphere coupling. Two primary physical mechanisms are attributed: (a) away from the magnetic equator, M2 horizontal winds penetrating directly into the thermosphere move plasma along vertically inclined magnetic field lines, and (b) close to the magnetic equator, M2 horizontal winds perturb E-region dynamo-driven electric fields and E × B particle drifts, thus imprinting upon the F-region electron density. Fig. 13 shows zonal winds at 114 km from the Michelson Interferometer for Global High-resolution Thermospheric Imaging (MIGHTI) on the NASA Ionospheric Connection (ICON) satellite and mapped into lunar local time (LLT) versus magnetic latitude (panel a) and the projection into M2 (panel b). The highest wind values are about 10 m/s, observed at the magnetic equator at 3 LLT. M2 undergoes nearly 180° phase shifts near 10°S and 15°N. Horizontal wind motions in the E-region induce charge separation by transporting collisional ions, while electrons gyrate about and translate along B. The resultant E is oriented upwind and drives E × B plasma drifts near the magnetic equator. For northward-pointing B, upward (downward) drift would result from height-integrated, conductivity-weighted westward (eastward) M2 zonal winds. Panel (c) shows the vertical component of the ICON Ion Velocity Meter (IVM) in-situ ion velocity perpendicular to local B. The 12-hr variation dominates the unfiltered drift. The M2 fit is shown in panel (d). The maximum upward (downward) drift is seen at 11 LLT at the magnetic equator, 2 h later than the westward (eastward) E-region M2 winds.

The leading role of E-region dynamo modulation in coupling solar and lunar tidal dynamics into the ionosphere is undisputed but there is growing evidence that other processes may play an important role, partly enabled by recent satellite missions such as ICON, Global-scale Observations of the Limb and Disk (GOLD), Constellation Observing System for Meteorology, Ionosphere and Climate (COSMIC) and COSMIC-2 (Immel et al., 2018; Eastes et al., 2017; Alexander et al., 2008; Randel et al., 2021). While *in situ* F-region ion drag has no measurable effect on the neutral "wave-4" in the upper thermosphere, models on the other hand suggest that tidal variations in thermospheric $[O]/[N_2]$ and meridional winds at F-region altitudes may add to the observed plasma variations, including effects from semidiurnal nonmigrating tides such as the SE2. Delineating and understanding these processes, including nonlinear interactions and secondary wave generation (described in detail below), is one challenge for the time to

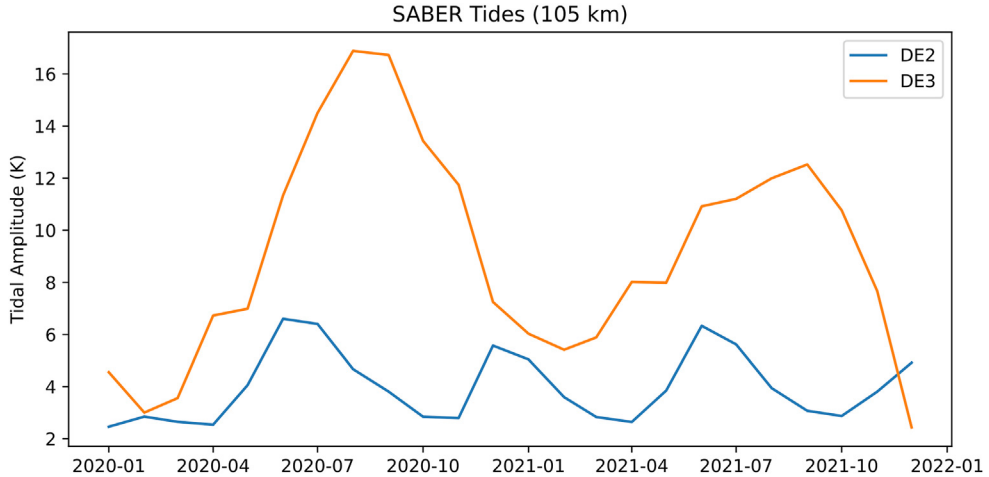

Fig. 12 Seasonal variation of the DE2 and DE3 temperature amplitudes near the equator (± 15° latitude) and 105 km altitude as observed by the TIMED/SABER instrument during 2020–2021. DE2 and DE3 appear as longitudinal wave-3 and wave-4, respectively, when observed in a LT frame.

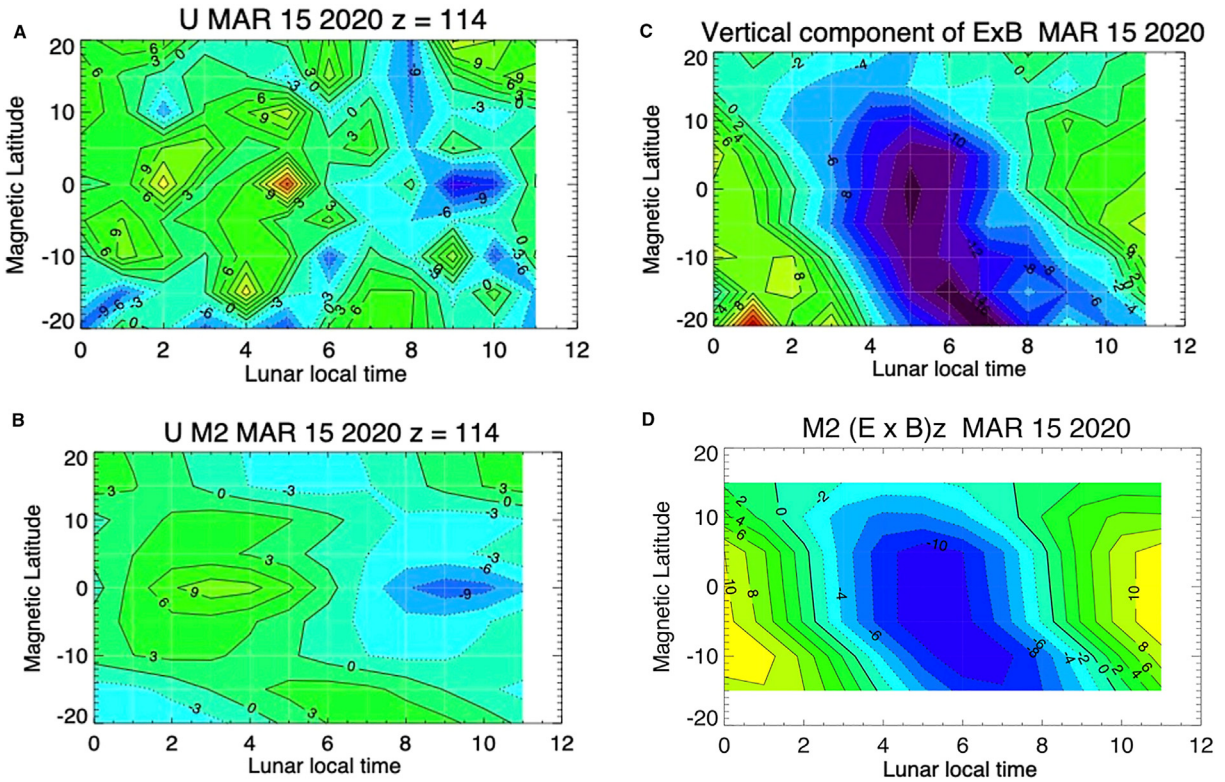

Fig. 13 (A) Michelson Interferometer for Global High-Resolution Thermospheric Imaging (MIGHTI) zonal winds at 114 km between 27 February and April 3, 2020 and mapped to magnetic latitude. (B) M2 fit to winds in panel (A). (C) Vertical component of ion velocity meter (IVM) plasma drift perpendicular to local (B) (D) M2 fit to drifts in panel (D). Reproduced with permission from Lieberman, R.S., Harding, B.J., Heelis, R.A., Pedatella, N.M., Forbes, J.M., Oberheide, J., 2022. Atmospheric lunar tide in the low latitude thermosphere-ionosphere. Geophys. Res. Lett. 49, e2022GL098078. https://doi.org/10.1029/2022GL098078.

come as tidal coupling from below constitutes a major energy term for the ionosphere-thermosphere system. An illustration of the main processes through which solar and lunar tides couple different atmospheric regions to the ionosphere is provided in **Fig. 14**. Vertically propagating secondary waves are produced through nonlinear interactions between tides and stationary planetary waves, traveling planetary waves, and ultra-fast Kelvin waves (UFKW) that, like tides, are mainly excited in the lower atmosphere. The modulated tidal spectrum dissipates between about 90 and 150 km, driving changes in the mean thermal, dynamical, and compositional structure of the thermosphere, and thus the ionosphere. Solar and lunar tidal winds move ionization with respect to the magnetic field (B) in the E-region to produce electric fields (E), currents (J), induced magnetic fields (ΔB), and layers of ionization, and redistribute ionization in the F-region along B. E-fields map unattenuated along B, redistribute F-region ionization through E $\times$ B drifts, and create the concentrations of ionization around $\pm 15°-20°$ magnetic latitudes from the EIA.

Nonlinear Wave-Wave Interactions

It is now well established that atmospheric tides can interact nonlinearly with each other and with longer-period global-scale waves, including planetary waves (PWs) and ultra-fast Kelvin waves (UFKW), to produce secondary waves that propagate from their source regions as independent waves, each contributing additional spatial-temporal variability to the IT system (Teitelbaum and Vial, 1991; Truskowski et al., 2014; Moudden and Forbes, 2013; Gasperini et al., 2015, 2022). Modulation of a tide by a longer period (2.5- to 20-day) global-scale wave occurs through a nonlinear quadratic interaction that results in the generation of "sum" and "difference" secondary waves. As illustrated in **Fig. 15**, the interaction between a global-scale wave with frequency σ_1 and zonal wavenumber s_1 and a tide with frequency σ_2 and zonal wavenumber s_2 yields sum and difference waves with frequencies $\sigma_1 \pm \sigma_2$ and zonal wavenumbers $s_1 \pm s_2$, respectively. Thus, the produced waves have sums and differences of the time frequencies and zonal wavenumbers, respectively, as their proper frequencies and zonal wavenumbers. Similarly, evidence also exists to support the theoretical prediction that two tides can interact to produce secondary waves that are also tides. Each secondary wave is affected differently by the background wind field depending on its zonal wavenumber and Doppler-shifted frequency. At some distance from the source, one of the secondary waves can be significantly larger than the other either due to propagation conditions or because the two waves are not excited with equal efficiency. Since a given

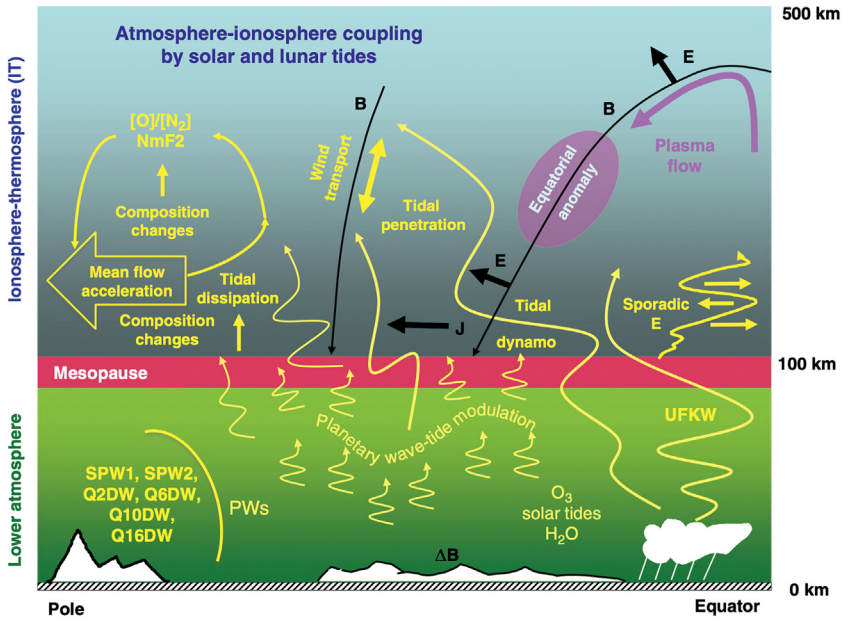

Fig. 14 Illustration of the main processes involved in atmosphere-ionosphere (A-I) coupling due to upward propagating solar and lunar tides. Reproduced with permission from Forbes, J.M., 2021. Atmosphere-ionosphere (A-I) coupling by solar and lunar tides. In Wang, W., Zhang, Y., Paxton, L.J. (Eds.), Space Physics And Aeronomy, vol. 4, Upper Atmosphere Dynamics And Energetics. American Geophysical Union, p. 560. ISBN: 978-1-119-50756-7.

global-scale wave can modulate several components of the tidal spectrum, each with a different period and zonal wavenumber, the resultant wave spectrum can become rather complex. A well-documented example of nonlinear wave-wave interaction is the modulation of the migrating (sun-synchronous, westward-propagating) semidiurnal tide (n = 2, s = 2) with the westward-propagating quasi-two-day wave (Q2DW, n = 0.5, s = 3). The sum and difference waves are a westward-propagating 9.6-h wave (n = 2.5) with s = 5 (n = 2.5, s = 5) and an eastward-propagating 16-h wave (n = 1.5) with s = −1. Another common example is the nonlinear interactions between non-migrating tides with UFKWs that produce secondary waves well capable of propagating to the middle and upper thermosphere and coupling into the ionosphere.

Tidal and wave diagnostics on middle thermospheric observations from the Gravity field and steady-state Ocean Circulation Explorer (GOCE) satellite indicate that vertical propagating waves together with sidebands from tidal-UFKW nonlinear interactions can be responsible for up to ∼60% of the total longitude and day-to-day variability of middle thermospheric density under solar low and geomagnetic quiet geophysical conditions (Gasperini et al., 2015). Additionally, modeling evidence suggests that a dissipating tidal spectrum modulated by global-scale waves causes the thermosphere to oscillate over a range of planetary-wave periods and that the same tidal spectrum can amplify penetration of westward propagating planetary waves into the thermosphere through nonlinear wave-wave interactions and cause similar oscillations in the ionosphere (Forbes et al., 2021).

Recent ICON observations, in conjunction with recent modeling capabilities, confirmed that nonlinear wave-wave interactions, including the secondary waves that arise from these interactions, play important roles in driving day-to-day ionospheric variability. Evidence suggests that secondary waves arising from Q2DW-tide, UFKW-tide, Q6DW-tide interactions are mainly excited below 100 km and that their exponential growth with height combined with molecular dissipation leads to secondary wave amplitude maxima in the 110−140 km height range. Secondary waves are themselves capable of carrying PW and UFKW periodicities into the ionosphere. Since the secondary waves occur with wave periods and zonal wavenumbers different than the primary interacting

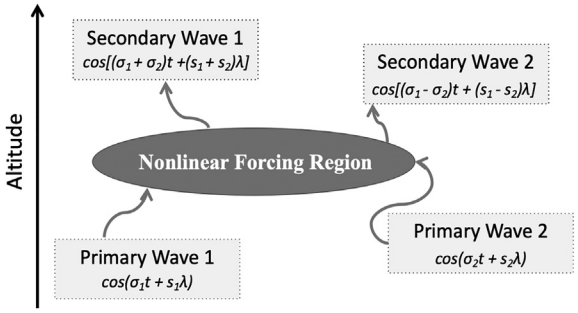

Fig. 15 Schematic of nonlinear interaction between two primary waves and the secondary waves therein produced.

waves, the aggregation of primary and secondary waves and their effects results in a degree of longitudinal and day-to-day variability much more complex than that from linear superposition of the primary waves alone.

Tidal Coupling on Inter-Seasonal and Intra-Seasonal Time Scales

Atmospheric tides are known to exhibit substantial temporal variability that extends from long (seasonal and inter-seasonal) to short (intra-seasonal and day-to-day) time scales (e.g., Sassi et al., 2019). The underlying mechanisms responsible for this variability involve the superposition of different Hough modes and changes in forcing conditions and propagation characteristics. For instance, the seasonal variation in DW1 is mainly driven by changes in tropospheric forcing in the (1,1) mode with additional effects due to background winds. E-region DW1 amplitudes generally display two maxima during the spring and fall equinoxes when heating is most efficient in the (1,1) mode due to equatorially symmetric solar irradiance at equinox. Mode coupling can occur due to vertical wind shears resulting in hemispheric asymmetries or contributions from different Hough modes.

The Quasi-Biannual Oscillation (QBO), the El Niño-Southern Oscillation (ENSO), and the solar cycle are the dominant modes of interannual variability in the atmosphere. The QBO is the characteristic mean flow behavior of zonal winds in the tropical stratosphere-mesosphere system, while ENSO is linked to periodic warming (El Niño phase) and cooling (La Niña phase) in western and central Pacific sea-surface temperatures resulting in changes in large-scale convective systems and redistribution of latent heat release and radiative heating. The QBO interaction with tides can dampen or enhance the tides as they propagate upwards to the ionosphere-thermosphere; while ENSO was shown to modify the forcing characteristics of tides, particularly non-migrating tides. The solar cycle is generally not considered to significantly affect vertically propagating tides in the E-region, likely due to the small solar cycle variations in the solar infrared emissions absorbed in the troposphere; however, it can significantly impact the propagation conditions of tides through the thermosphere due to the relationship between EUV heating and tidal dissipation.

Apart from seasonal and inter-annual variations, the tidal spectrum is known to exhibit large intra-seasonal to day-to-day variability. The Madden-Julian Oscillation (MJO) is a prominent eastward moving disturbance near the equator that recurs every about 30–90 days in winds, clouds, rainfall, and many other variables and is the dominant mode of intra-seasonal variability in tropical convection and circulation (Madden and Julian, 1971). Recent studies (e.g., Kumari et al., 2020, 2021) demonstrated that the tropospheric MJO can modulate the DE3 and DW1 temperature tides in the MLT by ~25% and ~10%, respectively (as illustrated in Fig. 16). The modulation of tidal heating is thought to be comparatively more important than the modulation of background winds to impose the MJO signal on the low-latitude MLT tides. Recent observational and modeling evidence also indicates that the MJO-modulated tidal spectrum extends well into the upper thermosphere (e.g., Gasperini et al., 2017, 2020) and is likely to produce significant impacts on the ionosphere.

The magnitude of the short-term day-to-day variability can be comparable to its long-term variability, and it has been shown that the diurnal tidal amplitude can vary by a factor of 2 to 3 from one day to the next, and some of this variability has been attributed to changes due to tidal-planetary wave interactions (Rajesh et al., 2021). A challenge in studying short-term tidal variability in the upper atmosphere is the lack of suitable global observations that allow resolving the tidal spectrum on a daily basis (the so-called "tidal weather"), as single satellite tidal diagnostics (such as those from TIMED and ICON) can only resolve tidal variations

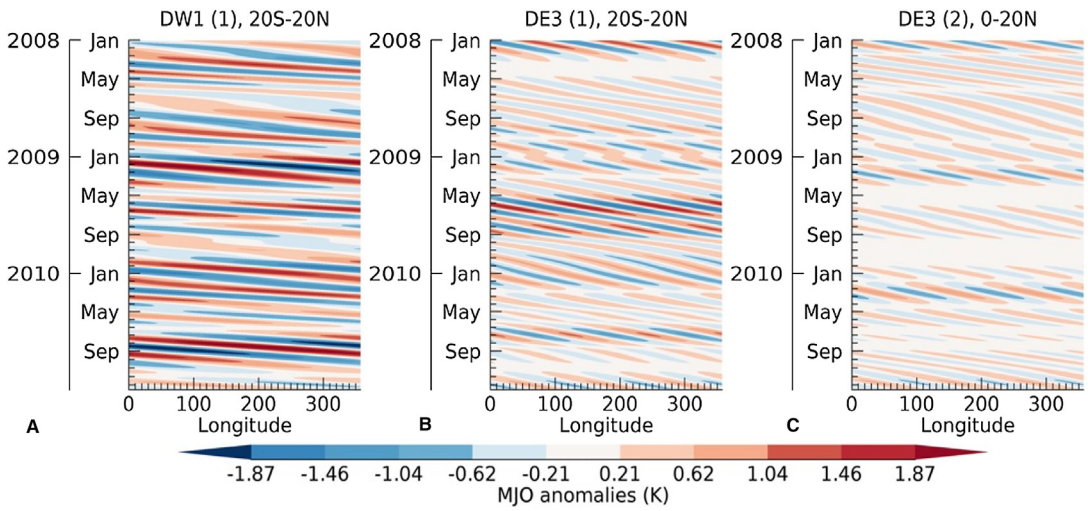

Fig. 16 Madden-Julian Oscillation (MJO)-modulation at 95 km of (A) the migrating diurnal tide DW1 averaged over the equator, (B) the nonmigrating DE3 (symmetric mode) (C) the DE3 asymmetric mode, from short-term tidal diagnostics of SABER/TIMED temperatures. Reproduced with permission from Kumari et al. (2021).

on a monthly or longer timescale (Oberheide et al., 2009, 2011; Gasperini et al., 2015, 2023a; Forbes et al., 2021). A well-studied source of short-term tidal variability in the atmosphere-ionosphere is due to changes in stratospheric and mesospheric polar vortex conditions, including the prominent Sudden Stratospheric Warmings (SSWs) discussed in detail below.

Atmosphere-Ionosphere Coupling via Tides during Stratospheric Sudden Warmings

SSWs are large-scale phenomena characterized by dramatic dynamic disruptions in the stratospheric winter polar regions associated with a weakening in the stratospheric polar vortex (Matsuno, 1971). SSWs cause large-scale variations in temperature, wind, and ozone density in the Arctic wintertime stratosphere at high latitudes and lead to considerable global impacts on the middle and upper atmosphere and ionosphere (**Fig. 17**) (Goncharenko and Zhang 2008; Chau et al., 2009; Butler et al., 2015; Pedatella and Liu, 2013, Pedatella et al. 2018; Gasperini et al., 2023b). SSWs represent one of the strongest manifestations of the coupling in the atmosphere-ionosphere system. Wind and temperature distributions during SSWs can generate background propagation conditions favorable for significant amplification of the M2 lunar tide. This enhancement has been attributed to a shifting of the Pekeris resonance peak to 12.42 h due to the altered background propagation conditions associated with SSWs (see Forbes and Zhang (2012) for more details). Solar tides are also significantly impacted by SSWs, especially semidiurnal tides, and the lunar and solar SSW-modulated tides can significantly impact both the E− and F-region ionosphere. In addition to weakened polar vortex conditions characteristic of SSWs, emerging modeling and observational studies suggest that exceptionally strong polar vortex conditions can lead to significant short-term variability in the IT system. As an example, **Fig. 18** shows SW2 amplitude in the zonal wind near 110 km from a whole atmosphere model during the NH winters of 1980−1981, 1982−1983, and 2008−2009, characterized by extended periods of enhanced stratospheric polar vortex. These periods are associated with a clear decrease in the SW2 tidal amplitude, especially in the northern hemisphere.

Open Questions

Atmospheric tides play a critical role in coupling terrestrial weather with space weather. Advancing the understanding of interconnections between different atmospheric regions and their effects on the ionosphere is uniquely tied to better characterizing atmospheric tides and their variability across different temporal scales through combined theoretical, modeling, and observational studies.

Variability of the tidal spectrum can be ascribed to changes in sources associated with tropospheric weather, variable propagation conditions, and nonlinear interactions. To this end, it is critical to identify the mechanisms that connect terrestrial variability with space weather on daily, sub-seasonal inter-annual scales and how they vary with altitude and geographic regions. Of particular importance is achieving a better understanding of how tides drive day-to-day and intra-seasonal variability in the ionosphere, and how the tidal spectrum changes due to nonlinear interactions with traveling planetary waves with periods of order 2−20 days and ultra-fast Kelvin waves (UFKWs) with periods of about 2−5 days. The secondary waves resulting from these nonlinear interactions have different periods and zonal wavenumbers than the primary interacting waves and thus can propagate away from their sources and penetrate effectively to different altitude-latitude regions than the primary waves. The spatial-temporal

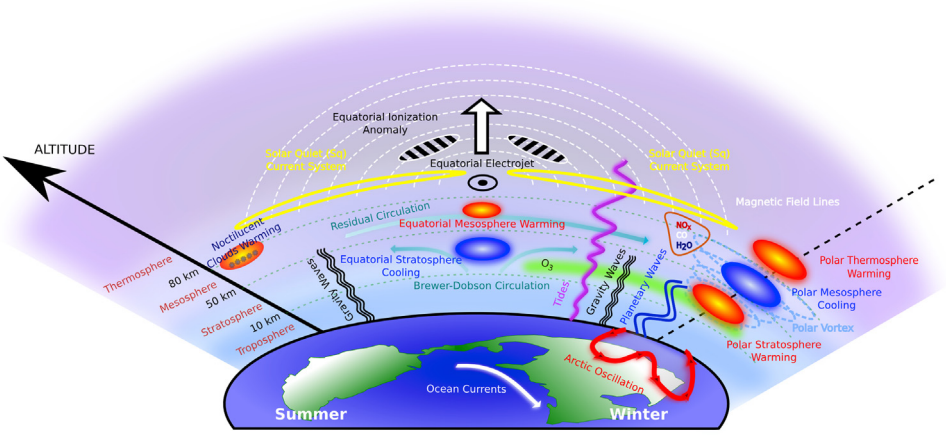

Fig. 17 Schematic of the coupling processes and atmospheric variability that occur during sudden stratospheric warming (SSW) events. Red and blue circles denote regions of warming and cooling, respectively. Reproduced with permission from Pedatella et al. (2018).

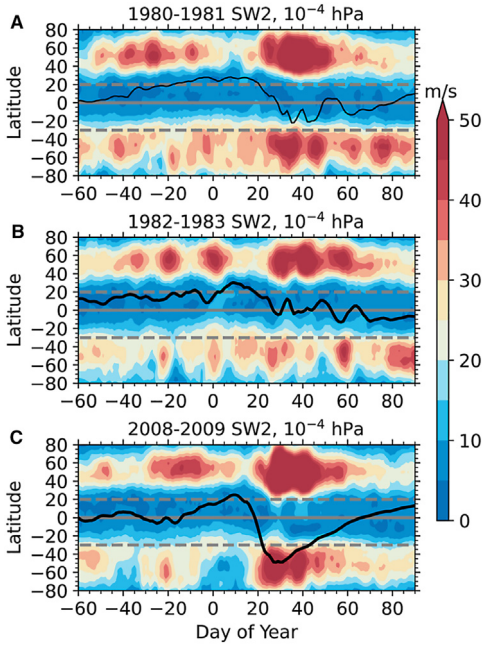

Fig. 18 SW2 amplitude in zonal wind at 10 − 4 hPa (∼110 km altitude) during the Northern Hemisphere winters (A) 1980–1981, (B) 1982–1983, and (C) 2008–2009. The thick black line is the Northern Annular Mode (NAM) index at 10 hPa multiplied by a factor of 10. Horizontal gray lines indicate a NAM of zero (solid) and the thresholds for defining the stratospheric polar vortex as strong (+2, dashed) and weak (−3, dashed). Reproduced with permission from Pedatella, N.M., Harvey, V.L., 2022. Impact of strong and weak stratospheric polar vortices on the mesosphere and lower thermosphere. Geophys. Res. Lett. 49, e2022GL098877. https://doi.org/10.1029/2022GL098877].

variability of the atmosphere-ionosphere coupling is significantly connected to these tidal-wave interaction processes. Related areas of research include better understanding (a) the factors that determine the characteristics and evolutions of primary and secondary waves resulting from the wave-wave interactions; (b) how the solar modulation of ionospheric conductivity due to tides may influence periodicities characteristic of the ionosphere; (c) the role of the magnetic field in determining the spectral response of the ionosphere to tides; (d) how the Madden-Julian Oscillation (MJO) affects tidal generation and propagation and hence the sub-seasonal variability of the whole atmosphere-ionosphere system.

Another important topic of active community interest is better understanding how changes to the stratospheric and mesospheric polar vortices lead to modifications in the solar and lunar tidal spectrum and thus affect the atmosphere-ionosphere coupling. It is now well established that polar vortex variability can lead to significant tidal amplification and suppression by the altered middle-atmosphere zonal mean state and excitation of nonmigrating tides through nonlinear interaction between quasi-stationary planetary waves and migrating tides at high latitudes. Penetration of the polar vortex-affected tidal spectrum above 100 km results in significant ionospheric modifications through the generation of dynamo electric fields in the E-region that redistribute F-region ionization through E x B drifts, tidal wind fields that penetrate to the F-region and transport ionization along magnetic field lines, and composition changes driven by dissipating tides that modify the zonal-mean ionospheric state. Outstanding questions in this area include: How do changes in the polar vortex lead to alterations in the whole atmosphere-ionosphere system and how do they depend on the strength of the polar vortex? How do they vary with altitude and geographic regions? What are the relative roles of solar and lunar tides in this connection? What are the effects of solar and geomagnetic preconditioning?

Despite recent improved observational capabilities afforded by missions, our ability to attain a comprehensive physical understanding of the processes at play is significantly impaired by the data sparsity in the ionosphere-thermosphere system. Without global measurements with sufficient temporal and spatial resolution, physics-based models cannot be validated, and data assimilation for these heights remains a tentative venture. The establishment and maintenance of suitable observing capabilities are thus critical to allow for the dynamical conditions to be monitored. The Geospace Dynamics Constellation (GDC) NASA mission is posed to provide critical observations to better understand ionosphere-thermosphere coupling processes involving atmospheric tides. Observations from the concurrent Dynamical Neutral Atmosphere-Ionosphere Coupling (DYNAMIC) mission will be particularly helpful by providing critical information on the height evolution of the tidal spectrum in the thermosphere. Synergistic measurements from GDC and DYNAMIC are expected to provide much-needed day/night wind, temperature, and composition tidal observations throughout the thermosphere and ionosphere on shorter time scales than previous missions. These observations will be critical for the effective investigation of wave-mean flow interactions, ion-neutral interactions, and dynamo processes involving atmospheric tides.

Supplementary Data

Supplementary data related to this article can be found online at https://doi.org/10.1016/B978-0-323-96026-7.00073-4

Acknowledgment

This article is a revision of the previous edition article by J Oberheide, M Hagan, J Forbes, A Richmond, volume 2, pp 287–297, © 2015, Elsevier Ltd.

References

Akmaev, R.A., Fuller-Rowell, T.J., Wu, F., Forbes, J.M., Zhang, X., Anghel, A.F., Iredell, M.D., Moorthi, S., Juang, H.-M., 2008. Tidal variability in the lower thermosphere: comparison of whole atmosphere model (WAM) simulations with observations from TIMED. Geophys. Res. Lett. 35, L03810. https://doi.org/10.1029/2007GL032584.

Alexander, S.P., Tsuda, T., Kawatani, Y., Takahashi, M., 2008. Global distribution of atmospheric waves in the equatorial upper troposphere and lower stratosphere: COSMIC observations of wave mean flow interactions. J. Geophys. Res. 113 (D24), D24115. https://doi.org/10.1029/2008JD010039.

Butler, A.H., Seidel, D.J., Hardiman, S.C., Butchart, N., Birner, T., Match, A., 2015. Defining sudden stratospheric warmings. Bull. Am. Meteorol. Soc. 96 (11), 1913–1928. https://doi.org/10.1175/bams-d-13-00173.1.

Chapman, S., Lindzen, R.S., 1970. Atmospheric Tides. Reidel, Dordrecht.

Chau, J.L., Fejer, B.G., Goncharenko, L.P., 2009. Quiet variability of equatorial E × B drifts during a sudden stratospheric warming event. Geophys. Res. Lett. 36, L05101.

Eastes, R.W., McClintock, W.E., Burns, A.G., et al., 2017. The global-scale observations of the Limb and Disk (GOLD) mission. Space Sci. Rev. 212, 383–408. https://doi.org/10.1007/s11214-017-0392-2.

England, S.L., Immel, T.J., Huba, J.D., Hagan, M.E., Maute, A., DeMajistre, R., 2010. Modeling of multiple effects of atmospheric tides on the ionosphere: an examination of possible coupling mechanisms responsible for the longitudinal structure of the equatorial ionosphere. J. Geophys. Res. 115, A05308. https://doi.org/10.1029/2009JA014894.

Fejer, J.A., 1964. Atmospheric tides and associated magnetic effects. Rev. Geophys. 2 (2), 275–309. https://doi.org/10.1029/RG002i002p00275.

Forbes, J.M., Lindzen, R.S., 1976a. Atmospheric solar tides and their electrodynamic effects-I. The global Sq current system. J. Atmos. Sol. Terr. Phys. 38, 897–910. https://doi.org/10.1016/0021-9169(76)90073-8.

Forbes, J.M., Lindzen, R.S., 1976b. Atmospheric solar tides and their electrodynamic effects-II. The equatorial electrojet. J. Atmos. Sol. Terr. Phys. 38, 911–920. https://doi.org/10.1016/0021-9169(76)90074-X.

Forbes, J.M., 1995. Tidal and planetary waves. Geophys. Monogr. 87, 67–87.

Forbes, J.M., Zhang, X., 2012. Lunar tide amplification during the January 2009 stratosphere warming event: observations and theory. J. Geophys. Res. 117, A12312. https://doi.org/10.1029/2012JA017963.

Forbes, J.M., Zhang, X., Heelis, R., Stoneback, R., Englert, C.R., Harlander, J.M., et al., 2021. Atmosphere-ionosphere (A-I) coupling as viewed by ICON: day-to-day variability due to planetary wave (PW)-tide interactions. J. Geophys. Res. Space Phys. 126, e2020JA028927. https://doi.org/10.1029/2020JA028927.

Gasperini, F., Forbes, J.M., Doornbos, E.N., Bruinsma, S.L., 2015. Wave coupling between the lower and middle thermosphere as viewed from TIMED and GOCE. J. Geophys. Res. Space Phys. 120, 5788–5804. https://doi.org/10.1002/2015JA021300.

Gasperini, F., Hagan, M.E., Zhao, Y., 2017. Evidence of tropospheric 90-day oscillations in the thermosphere. Geophys. Res. Lett. 44, 10,125–10,133. https://doi.org/10.1002/2017GL075445.

Gasperini, F., Liu, H., McInerney, J., 2020. Preliminary evidence of Madden-Julian Oscillation effects on ultrafast tropical waves in the thermosphere. J. Geophys. Res.: Space Phys. 125, e2019JA027649. https://doi.org/10.1029/2019JA027649.

Gasperini, F., Crowley, G., Immel, T.J., Harding, B.J., 2022. Vertical wave coupling in the low-latitude Ionosphere-Thermosphere as revealed by concurrent ICON and COSMIC-2 Observations. Space Sci. Rev. 218 (7), 55. https://doi.org/10.1007/s11214-022-00923-1.

Gasperini, F., Harding, B.J., Crowley, G., Immel, T.J., 2023a. Ionosphere-thermosphere coupling via global-scale waves: new insights from two-years of concurrent in situ and remotely-sensed satellite observations. Front. Astron. Space Sci. 10, 1217737. https://doi.org/10.3389/fspas.2023.1217737.

Gasperini, F., Jones Jr., M., Harding, B.J., Immel, T.J., 2023b. Direct observational evidence of altered mesosphere lower thermosphere mean circulation from a major sudden stratospheric warming. Geophys. Res. Lett. 50, e2022GL102579. https://doi.org/10.1029/2022GL102579.

Goncharenko, L., Zhang, S.R., 2008. Ionospheric signatures of sudden stratospheric warming: ion temperature at middle latitude. Geophys. Res. Lett. 35, L21103.

Hagan, M.E., Forbes, J.M., Vial, F., 1995. On modeling migrating solar tides. Geophys. Res. Lett. 22, 893–896.

Hagan, M.E., Maute, A., Roble, R.G., Richmond, A.D., Immel, T.J., England, S.L., 2007. Connections between deep tropical clouds and the Earth's ionosphere. Geophys. Res. Lett. 34, L20109. https://doi.org/10.1029/2007GL030142.

Immel, T.J., Sagawa, E., England, S.L., Henderson, S.B., Hagan, M.E., Mende, S.B., Frey, H.U., Swenson, C.M., Paxton, L.J., 2006. Control of equatorial ionospheric morphology by atmospheric tides. Geophys. Res. Lett. 33, L15108. https://doi.org/10.1029/2006GL026161.

Immel, T.J., England, S.L., Mende, S.B., et al., 2018. The ionospheric connection explorer mission: mission goals and design. Space Sci. Rev. 214, 13. https://doi.org/10.1007/s11214-017-0449-2.

Kumari, K., Oberheide, J., Lu, X., 2020. The tidal response in the mesosphere/lower thermosphere to the Madden-Julian oscillation observed by SABER. Geophys. Res. Lett. 47, e2020GL089172. https://doi.org/10.1029/2020GL089172.

Kumari, K., Wu, H., Long, A., Lu, X., Oberheide, J., 2021. Mechanism studies of Madden- Julian-oscillation coupling into the mesosphere/lower thermosphere tides using SABER, MERRA-2 and SD-WACCMX. J. Geophys. Res. Atmos. 126, e2021JD034595. https://doi.org/10.1029/2021JD034595.

Liu, H., Yamamoto, M., Lühr, H., 2009. Wave-4 pattern of the equatorial mass density anomaly: a thermospheric signature of tropical deep convection. Geophys. Res. Lett. 36, L18104. https://doi.org/10.1029/2009GL039865.

Madden, R.A., Julian, P.R., 1971. Detection of a 40–50 Day oscillation in the zonal wind in the tropical Pacific. J. Atmos. Sci. 28, 702–708.

Matsuno, T., 1971. A dynamical model of the stratospheric sudden warming. J. Atmos. Sci. 28, 1479–1494.

Matsushita, S., 1967a. Solar quiet and lunar daily variation fields. In: Matsushita, S., Campbell, W.H. (Eds.), Physics of Geomagnetic Phenomena. Academic Press, New York, pp. 301–427.

Matsushita, S., 1967b. Lunar tides in the ionosphere. In: Handbuch der Physik. Springer-Verlag, Berlin, pp. 547–602.

Moudden, Y., Forbes, J.M., 2013. A decade-long climatology of terdiurnal tides using TIMED/SABER observations. J. Geophys. Res.: Space Phys. 118, 4534–4550. https://doi.org/10.1002/jgra.50273.

Oberheide, J., Forbes, J.M., Häusler, K., Wu, Q., Bruinsma, S.L., 2009. Tropospheric tides from 80 to 400 km: propagation, interannual variability, and solar cycle effects. J. Geophys. Res. 114, D00I05. https://doi.org/10.1029/2009JD012388.

Oberheide, J., Forbes, J.M., Zhang, X., Bruinsma, S.L., 2011. Wave-driven variability in the ionosphere—thermosphere—mesosphere system from TIMED observations: what contributes to the "wave-4"? J. Geophys. Res. 116, A01306. https://doi.org/10.1029/2010JA015911.

Oberheide, J., Hagan, M.E., Richmond, A.D., Forbes, J.M., 2015. Dynamical meteorology j atmospheric tides. In: North, G.R., Pyle, J., Zhang, F. (Eds.), Encyclopedia of Atmo-Spheric Sciences. Academic Press, Oxford, pp. 287—297. https://doi.org/10.1016/B978-0-12-382225-3.00409-6.

Pedatella, N.M., Liu, H.-L., 2013. The influence of atmospheric tide and planetary wave variability during sudden stratosphere warmings on the low latitude ionosphere. J. Geophys. Res. 118, 5333—5347. https://doi.org/10.1002/jgra.50492.

Pedatella, N.M., Chau, J.L., Schmidt, H., Goncharenko, L.P., Stolle, C., Hocke, K., Harvey, V.L., Funke, B., Siddiqui, T.A., 2018. How sudden stratospheric warming affects the whole atmosphere. EOS 99, 35—38.

Rajesh, P.K., Lin, C.H., Lin, J.T., Lin, C.Y., Yue, J., Matsuo, T., Chen, S.P., 2021. Day-to- day variability of ionosphere electron density during solar Minimum derived from FORMOSAT-7/COSMIC-2 measurements. Terr. Atmos. Ocean Sci. https://doi.org/10.3319/TAO.2021.08.01.01. http://tao.cgu.org.tw/index.php/articles/archive/space- science/item/1779-2021080101f7c2.

Randel, W.J., Wu, F., Podglajen, A., 2021. Equatorial waves, diurnal tides and small-scale thermal variability in the tropical lower stratosphere from COSMIC-2 radio occultation. J. Geophys. Res. Atmos. 126, e2020JD033969. https://doi.org/10.1029/2020JD033969.

Richmond, A.D., 1971. Tidal winds at ionospheric heights. Radio Sci. 6 (2), 175—189. https://doi.org/10.1029/RS006i002p00175.

Richmond, A.D., 1995. The ionospheric wind dynamo: effect of its coupling with different atmospheric regions. In: Johnson, R.M., Killeen, T.L. (Eds.), The Upper Mesosphere and Lower Thermosphere: A Review of Experiment and Theory. Geophysical Monograph 87. American Geophysical Union.

Sassi, F., McCormack, J.P., McDonald, S.E., 2019. Whole atmosphere coupling on intraseasonal and interseasonal time scales: a potential source of increased predictive capability. Radio Sci. 54, 913—933. https://doi.org/10.1029/2019RS006847.

Scherliess, L., Thompson, D.C., Schunk, R.W., 2008. Longitudinal variability of low-latitude total electron content: tidal influences. J. Geophys. Res. 113, A01311. https://doi.org/10.1029/2007JA012480.

Tarpley, J.D., 1970a. The ionospheric wind dynamo,1, Lunar tides. Planet. Space Sci. 18, 1075—1090.

Tarpley, J.D., 1970b. The ionospheric wind dynamo, 2, Solar tides. Planet. Space Sci. 18, 1091—1103.

Teitelbaum, H., Vial, F., 1991. On tidal variability induced by nonlinear interaction with planetary waves. J. Geophys. Res. 96, 14169—14178.

Truskowski, A.O., Forbes, J.M., Zhang, X., Palo, S.E., 2014. New perspectives on thermosphere tides - 1. Lower thermosphere spectra and seasonal-latitudinal structures. Earth Planets Space 66, 136. https://doi.org/10.1186/s40623-014-0136-4.

Vial, F., Forbes, J.M., 1994. Monthly simulations of the lunar semi-diurnal tide. J. Atmos. Sol. Terr. Phys. 56, 1591—1607.

Zhang, J.T., Forbes, J.M., 2013. Lunar tidal winds between 80 and 110 km from UARS/HRDI wind measurements. J. Geophys. Res. 118 (8), 5296—5304. https://doi.org/10.1002/jgra.50420.

Further Reading

Chapman, S., Bartels, J., 1940. Geomagnetism. Clarendon Press, Oxford.

Haurwitz, B., Cowley, A.D., 1973. The diurnal and semidiurnal oscillations, global distribution and annual variation. Pure Appl. Geophys. 102, 193—222.

Liu, H.-L., 2016. Variability and predictability of the space environment as related to lower atmosphere forcing. Space Weather 14, 634—658. https://doi.org/10.1002/2016SW001450.

Schindelegger, M., Sakazaki, T., Green, M., 2023. Atmospheric tides—an Earth system signal. In: A Journey through Tides. Elsevier, pp. 389—416.

Volland, H., 1988. Atmospheric Tidal and Planetary Waves. Kluwer Academic, Dordrecht.

Yiğit, E., Knízova, P.K., Georgieva, K., Ward, W., 2016. A review of vertical coupling in the atmosphere-ionosphere system: effects of waves, sudden stratospheric warmings, space weather, and of solar activity. J. Atmos. Sol. Terr. Phys. 141, 1—12. https://doi.org/10.1016/j.jastp.2016.02.011.